This article has been accepted for publication in a future issue of this journal, but has not been fully edited. Content may change prior to final publication. Citation information: DOI 10.1109/TSTE.2019.2890828, IEEE Transactions on Sustainable Energy

Grid-Connected Wind-Photovoltaic Cogeneration Using Back-to-Back Voltage Source Converters

Amr Ahmed A. Radwan, *Member, IEEE* and Yasser Abdel-Rady I. Mohamed*, Senior Member, IEEE*

***Abstract*—This paper introduces a new topology, yet simple and efficient, for a grid-connected wind-photovoltaic (PV) cogeneration system. A permanent magnet synchronous generator-based full-scale wind turbine is interfaced to the utility-grid via back-to-back (BtB) voltage-source converters (VSCs). A PV solar generator is directly connected to the dc-link capacitor of the BtB VSCs. No dc/dc conversion stages are required, and hence the system efficiency is maximized. The proposed topology features an independent maximum power point tracking for both the wind and the PV generators to maximize the extraction of the renewable energy. The regulation of the VSCs is achieved via the vector control scheme in the rotating reference frame. The detailed small-signal models for the system components are developed to investigate the overall stability. The influence of the utility-grid faults on the performance of the proposed system is also evaluated. Nonlinear time-domain simulation results under different operating conditions are presented to validate the effectiveness of the proposed topology.**

***Index Terms*--AC-DC power converters, DC-AC power converters, maximum power point trackers, permanent magnet machines, solar power generation, wind power generation.**

I. Introduction

The cost of the wind and solar energy generation has been rapidly falling since the last decade. Driven by their economic and technical incentives, the global installed capacity of photovoltaic (PV) and wind generators has approached 303 Gigawatt (GW) and 487 GW in 2016, as compared to 6 GW and 74 GW in 2006, respectively [1].

Due to the intermittent and unregulated nature of the wind and solar energy, power-electronic converters are utilized as an interfacing stage to the load-side or the utility-grid, and hence distributed generation units are created [2]-[3]. In literature, most of the distributed generation systems are solely dedicated for one form of renewable resources, e.g., a solar energy as in [4]-[5] or a wind energy as in [6]-[8].

In order to maximize the benefits of the available renewable resources, the combination of the wind and solar energy in the same vicinity has been considered [9]-[22]. The cogeneration of the wind and solar energy has the following characteristics; 1) the availability of the wind and solar energy is generally complementary, and hence combining both forms of energy increases the overall operational efficiency [23]. 2) the combination of the wind and solar co-generators optimizes the utilization of lands resources, and hence improves the capital investments [24]. 3) as compared to the static PV generators, the wind-solar cogeneration systems are more dynamically capable to support the utility-grid due to the available moment of inertia in the mechanical system of the wind generators [8]. 4) having two sources of energy increases the generation reliability [9]-[10].

The grid-connected wind-PV cogeneration systems are not widely addressed [9]-[15]. On the contrary, several wind-PV cogeneration systems are proposed for the standalone off-grid applications [10], [16]-[22].

A standalone wind-PV cogeneration system is proposed in [16]-[17]. On the small-scale level, a single-phase cogeneration system has been proposed in [18] whereas a laboratory-scale system is introduced in [19]-[20]. Generally, the system structure in [16]-[20] comprises a common dc-bus that interfaces several parallel connected converters-interfaced renewable energy resources, which might reduce the overall system efficiency and increase the cost [12]. More importantly, the cascaded connection of power converters requires rigorous controllers coordination to avoid the induced interactions dynamics, which might yield instabilities [25]-[26]. A back-to-back (BtB) voltage-source converter (VSC) connected to a doubly-fed induction generator is used to interface a dc-dc converter-interfaced PV generator and an energy storage unit in [21]. In [22], a PV generator charging a battery bank and interfaced to a wind driven induction generator via a VSC is proposed. The wind-PV cogeneration systems in [21]-[22] highlights the efficient integration of the renewable energy resources with the minimal utilization of power-electronic conversion stages. However, these systems are proposed for specific off-grid applications.

In [12]-[14], the utility-grid integration of the renewable energy resources has been improved by using multiple-input converters. A buck/buck-boost fused dc-dc converter is proposed in [12]. A dc-dc converter with a current-source interface, and a coupled transformer is proposed in [13] and [14], respectively. However, the proposed systems in [12]-[14] are based on the dc power distribution which might not be the ideal distribution medium in the ac-dominated power systems.

Up to the authors' best knowledge, the combination of the grid-connected wind-PV systems has been solely addressed in [15]. The system in [15] comprises a BtB VSCs to interface the PV and wind generators to the utility-grid. On the machine-side-VSC, the dc-link voltage is regulated to the maximum power-point tracking (MPPT) value of the PV panels by an outer loop proportional-and-integral (PI) dc voltage controller. The reference values of the machine-side currents are calculated using the synchronous detection method, and a hysteresis current controller is utilized for the regulation. On the grid-side-VSC, a

A. Radwan is with the Engineering and Design Department, Western Washington University, Bellingham, WA 98225, USA (email: amr.radwan@ieee.org).

Y. Mohamed is with the Department of Electrical and Computer Engineering, University of Alberta, Edmonton, AB T6G2V4, Canada (email: yasser2@ualberta.ca).

This article has been accepted for publication in a future issue of this journal, but has not been fully edited. Content may change prior to final publication. Citation information: DOI 10.1109/TSTE.2019.2890828, IEEE Transactions on Sustainable Energy

hysteresis grid-current controller is used to inject the total currents into the utility-grid. In spite of the potential benefits of the proposed system in [15], the following challenges are noted; 1) the MPPT of either the PV and wind power involves the operation of both VSCs, which in some cases might decreases the system reliability and increases the losses. For instance, if the wind velocity is lower than the cut-off speed of the wind turbine, i.e., no wind power, the machine-side VSC may be unable to track the solar PV MPPT dc-link voltage [15]. 2) the currents of the machine and grid-side converters are regulated using hysteresis controllers resulting in a variable switching frequency and higher harmonic contents.

Motivated by the promising benefits of the wind-PV generation systems, this paper introduces a new topology, yet simple and efficient to interface both the wind and PV generators into the utility-grid. The contributions of this paper are as following;

1) The realization of the grid-connected wind-PV cogeneration system using BtB VSCs with no extra dc/dc conversion stages.
2) Independent MPPT operation where the MPPT of the wind and PV generators is solely achieved by the voltage-source rectifier (VSR), and the voltage-source inverter (VSI), respectively.
3) The development of the complete small-signal state-space model of the wind-PV cogeneration system to characterize the overall system stability.
4) The performance of proposed system has been investigated under different operating conditions, including the utility-grid faults, using time-domain simulations.

II. Modeling and Control of the Proposed Wind-Photovoltaic Cogeneration System

As shown in Fig. 1, the proposed system consists of a VSR to interface the wind generator, and a VSI to connect the cogeneration system into the utility-grid. The PV generator is directly connected to the dc-link capacitor of the BtB VSCs via a dc cable [27]. The VSR and VSI are two-level converters consisting of six cells; each comprises an insulated-gate-bipolar-transistor (IGBT) in parallel with a diode.

In the following subsections, the complete modeling and control of the proposed system is provided.

A. Wind Generator

A full-scale wind turbine (FSWT) utilizing a permanent magnet synchronous generator (PMSG) is selected for its low maintenance and low operational cost [2]. The wind turbine model is represented as following,

$$P_m = \frac{1}{2} C_p(\mathcal{B}, \lambda) \rho \pi R^2 v_{wind}^3, \qquad \lambda = \frac{R\omega_r}{v_{wind}} \tag{1}$$

where P_m is the mechanical power captured by the wind turbine blades; C_p is the rotor coefficient which is a non-linear function of the blade pitch angle ($\mathcal{B}$) and the tip-speed ratio (λ); ρ is the air density; R is the radius of the wind turbine blade; v_{wind} is the wind speed; and ω_r is the mechanical speed of the rotor. In this paper, $\mathcal{B}$ is set to zero in the normal operating conditions to maximize the wind power generation [13]. The PMSG is modeled as following,

$$\bar{v}_s = R_s \bar{\imath}_s + L_s \frac{d\bar{\imath}_s}{dt} + j\mathcal{P}\omega_r(\psi + L_s \bar{\imath}_s) \tag{2}$$

$$J\frac{d}{dt}\omega_r + \beta\omega_r = \frac{3}{2}\mathcal{P}\psi I_{sq} - T_m \tag{3}$$

In (2), $\bar{v}_s$ and $\bar{\imath}_s$ are the stator voltage and current in the complex vectors representation, respectively, where a complex vector $\bar{x} = X_d + jX_q$ such that X_d and X_q are the direct ($d-$) and quadrature ($q-$) components of $\bar{x}$ in the rotating reference frame; R_s and L_s are the stator-winding resistance and inductance, respectively; j is the imaginary unit number; ψ is the flux linkage of the rotor magnets; $\mathcal{P}$ is the number of poles pairs; T_m is the mechanical torque; whereas J and β are the motor inertia, and viscous friction, respectively.

B. Machine-Side Voltage Source Rectifier (VSR)

Fig. 2 shows the relationship between the mechanical rotor speed and the generated wind-turbine power at different wind speeds. At any wind speed, there is an optimal value of the mechanical rotor speed that corresponds to the generation of the maximum wind power. The extraction of the maximum wind power is achieved by the VSR in Fig. 1. The MPPT algorithm for the wind generator (MPPT_w) uses the wind speed (v_w) to generate the optimal value of the rotor speed (ω_r^*) following the mechanical characteristics in Fig. 2 [17], [19].

As shown in (4), a PI speed controller ($G_s(s) = g_{ps} + g_{is}/s$) is implemented to regulate the rotor speed (ω_r) to the optimal value (ω_r^*) and dictates the q-component of stator current reference (I_{sq}^*), whereas the d-component of stator current reference (I_{sd}^*) is set to zero to operate at the maximum produced torque [19].

$$I_{sq}^* = (\omega_r^* - \omega_r)G_s(s), \qquad I_{sd}^* = 0 \tag{4}$$

where s represents the differential operator.

Solving (3) and (4), assuming $I_{sq} \approx I_{sq}^*$ within the bandwidth of the speed controller ($G_s(s)$), and setting $g_{is}/g_{ps} = \beta/J$, the closed-loop transfer-function of the speed controller becomes; $\omega_r/\omega_r^* = \left(\frac{3}{2}\mathcal{P}\psi g_{ps}/J\right)/\left(s + \left(\frac{3}{2}\mathcal{P}\psi g_{ps}/J\right)\right)$, where the bandwidth is $\frac{3}{2}\mathcal{P}\psi g_{ps}/J$ [rad/s], and is selected to be around 10% of the bandwidth of the inner current controller [discussed in the following paragraph]. The speed controller parameters, i.e., g_{ps} and g_{is}, can be tuned accordingly.

As shown in Fig. 1 and (5), a PI current controller ($G_i(s) = g_{pi} + g_{ii}/s$) is employed so that the generated stator currents of the PMSG follow the corresponding references in (4).

$$\bar{v}_s = (\bar{\imath}_s^* - \bar{\imath}_s)G_i(s) + j\mathcal{P}\omega_r^{\circ} L_s \bar{\imath}_s + j\mathcal{P}\psi H\omega_r \tag{5}$$

where $j\mathcal{P}\omega_r^{\circ} L_s \bar{\imath}_s$ are the decoupling loops; H is a gain; whereas the superscript "$\circ$" denote the steady-state value of the variable. The current controller in (5) is designed by solving (2) and (5). By setting $g_{ii}/g_{pi} = R_s/L_s$, the closed loop transfer function of the current controller becomes; $I_{sd}/I_{sd}^* = 1/(\tau_i s + 1)$, where the bandwidth of the current controller is $1/\tau_i = g_{pi}/L_s$ [rad/s], and is selected to be around 10-20% of the switching frequency of the VSR.

This article has been accepted for publication in a future issue of this journal, but has not been fully edited. Content may change prior to final publication. Citation information: DOI 10.1109/TSTE.2019.2890828, IEEE Transactions on Sustainable Energy

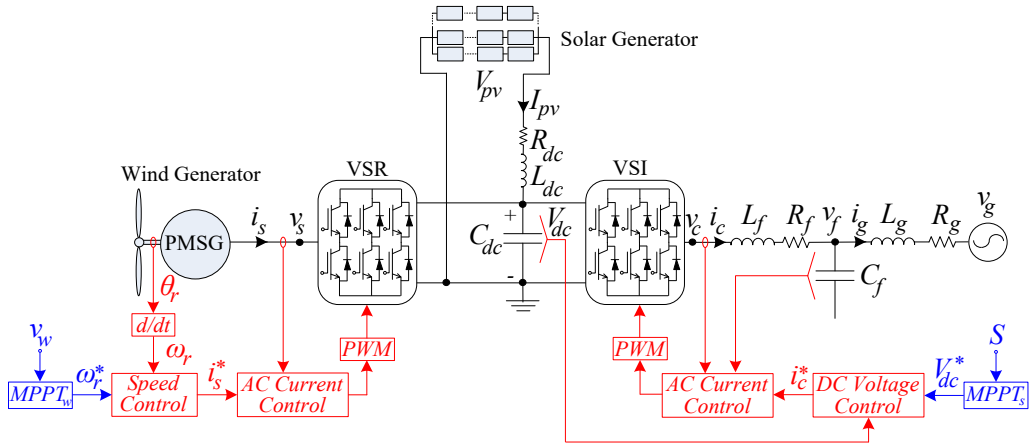

Fig. 1. The proposed wind-PV cogeneration system.

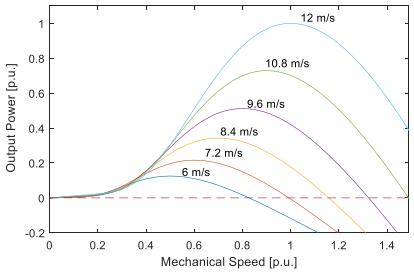

Fig. 2. Mechanical characteristics of the wind turbine at different wind speeds.

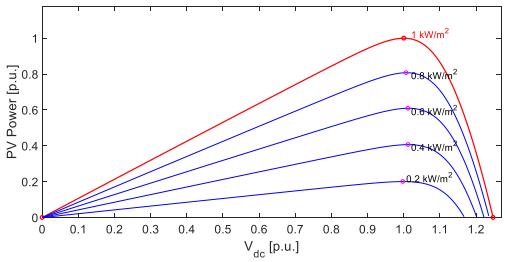

Fig. 3. $I_{pv} - V_{pv}$ characteristics of the PV array at different solar irradiance levels.

C. Photovoltaic Generator

In this paper, a PV array of a model "PV-UD190MF5" has been considered [28]. The PV model is highly-nonlinear but reflects no dynamic performance on the transient stability of the system. The model of the PV generator is given in Appendix A whereas the dc cable dynamics in Fig. 1 are modeled as following;

$$V_{pv} = V_{dc} + R_{dc} I_{pv} + L_{dc} \frac{dI_{pv}}{dt} \tag{6}$$

The I_{pv}-V_{pv} characteristics of the PV array are shown in Fig. 3. At any solar irradiance level, there is an optimal operating point (I_{pv}°, V_{pv}°) corresponding to the maximum generated PV power. As shown in Fig. 1, the MPPT algorithm of the PV array (MPPT_s) uses the solar irradiance level (S) to determine the optimal value of the dc-link voltage (V_{dc}^*) [from Fig. 3] that corresponds to the generation of the maximum PV power [4].

Referring to Fig. 1, the nominal voltage for PV arrays is designed at 1457V. With nowadays improvements in the centralized power converters, PV arrays can be directly connected to a dc-link with nominal dc voltage up to 1500V at 2.0 MVA [29].

D. Grid-Side Voltage Source Inverter (VSI)

As shown in Fig. 1, the ac-side of the VSI is terminated by an inductive filter (L_f) with an internal resistance (R_f) and a shunt capacitor (C_f). The root-mean-square (rms) value of the three-phase terminal voltage and currents of the VSI are v_c and i_c, respectively. The utility-grid-impedance comprises an inductive part (L_g) in series with the equivalent resistance of the line (R_g); v_g and i_g are the utility-grid three-phase rms voltage and currents, respectively.

The L_f-C_f filter and the utility-grid impedance are modelled as following;

$$\bar{v}_c = \bar{v}_f + R_f \bar{\imath}_c + L_f \frac{d\bar{\imath}_c}{dt} + j\omega L_f \bar{\imath}_c \tag{7}$$

$$\bar{v}_f = \bar{v}_g + R_g \bar{\imath}_g + L_g \frac{d\bar{\imath}_g}{dt} + j\omega L_g \bar{\imath}_g \tag{8}$$

$$\bar{\imath}_c = C_f \frac{d\bar{v}_f}{dt} + \bar{\imath}_g + j\omega C_f \bar{v}_f \tag{9}$$

To avoid the over-modulation of the VSI, the design of the PV array should consider the coordination between the MPPT voltage of the PV array, i.e., V_{dc}, and the rms voltage at the point-of-common coupling (PCC), i.e., v_f, under all irradiance levels. In power converters, the pulse-width–modulation (PWM) and the switching pattern is dictated by the ratio between the ac and the dc voltage such that $\bar{v}_c = \bar{m}\, V_{dc}/2$, where $\bar{m}$ is the modulation signal in complex vectors. As $\bar{v}_c$ is relatively constant, and so $\bar{v}_f$ under the steady-state conditions, then any major variations in V_{dc} might induce an over-modulated operation or a poor dc-link utilization, which in turns degrades the injected power quality into the utility-grid. Referring to Fig. 3, V_{dc} ranges from 0.997 to 1.012p.u. at zero to fully-rated irradiance level, respectively. Clearly, this is a slight variation in the dc-link voltage under the wide spectrum of the irradiance levels, and so the corresponding influence on the injected power quality and the switching pattern is minimal.

The VSI is regulated by the vector control scheme where a phase-locked-loop (PLL) is used to synchronize the converter with the utility-grid [30]. In (10), a PI controller ($G_\delta(s) = K_{p\delta} + K_{i\delta}/s$) is implemented in the PLL structure to set the q-component of the PCC voltage (V_{cq}) to zero and generate the synchronization angle $\delta(t)$, where $\delta(t) = \int \omega(t)dt$. Under transient conditions, the angle $\delta(t)$ oscillates to resynchronize

This article has been accepted for publication in a future issue of this journal, but has not been fully edited. Content may change prior to final publication. Citation information: DOI 10.1109/TSTE.2019.2890828, IEEE Transactions on Sustainable Energy

the converter with the utility-grid and eventually becomes zero in the steady-state conditions.

$$\omega = \omega^{\circ} + \frac{V_{fq}^{c}}{V_{fd}^{\circ}} K_{\delta}(s) \tag{10}$$

As shown in (11), the main advantage of the vector control is the decoupling between the active and reactive power regulation. As V_{cq} is set to zero by (10) and assuming V_{cd} is constant, the active power injection from the VSI (P_{vsi}) can be regulated by controlling I_{cd} whereas the reactive power (Q_{vsi}) is solely dependent on I_{cq}.

$$\begin{aligned} P_{vsi} &= Real\{1.5\bar{v}_c\bar{\imath}_c^{conjugate}\} = 1.5V_{cd}I_{cd}, \\ Q_{vsi} &= Imaginary\{1.5\bar{v}_c\bar{\imath}_c^{conjugate}\} = -1.5V_{cd}I_{cq} \end{aligned} \tag{11}$$

In conclusion, the roles of the VSI in the proposed system are;

1) *DC-Link Voltage Control*:

The dc-link voltage of the BtB VSCs (V_{dc}) is regulated to the optimal value (V_{dc}^{*}) [generated by MPPT$_s$] as shown in (12), where a PI dc voltage controller ($K_{dc}(s) = k_{pdc} + k_{idc}/s$) is implemented.

$$I_{cd}^{*} = -(V_{dc}^{*2} - V_{dc}^{2})K_{dc}(s)\left(\frac{1}{1.5V_{fd}^{\circ}}\right) \tag{12}$$

Referring to Fig. 1, and as shown in (13), the rate of change of the energy in C_{dc} is governed by the balance between the delivered wind and PV power ($P_{wind} + P_{pv}$) and the injected active power to the utility-grid (P_{vsi}), assuming a lossless converter.

$$\frac{1}{2}C_{dc}\frac{d}{dt}V_{dc}^{2} = P_{wind} + P_{pv} - P_{vsi} \tag{13}$$

where $P_{wind} = Real\{1.5\bar{v}_s\bar{\imath}_s^{conjugate}\}$ and $P_{solar} = V_{dc}I_{pv}$.

By regulating V_{dc} in (12), the input, i.e., $P_{wind} + P_{pv}$, and the output, i.e., P_{vsi}, active powers are balanced in (13), and so the active power component (I_{cd}^{*}) is generated from (12).

Using (11)-(13), the open-loop transfer function of the dc-link voltage controller becomes; $l_{vdc}(s) = \left(2k_{pdc}/\tau_k C_{dc}\right)\left(\left(s + \frac{k_{idc}}{k_{pdc}}\right)\Big/\left(s + \frac{1}{\tau_k}\right)\right)\frac{1}{s^2}$, where $\frac{1}{\tau_k}$ is the bandwidth of the inner current controller of the VSI. Note that the $l_{vdc}(s)$ has three poles; two at zero and one at $-\frac{1}{\tau_k}$. At low frequencies, the phase angle of $l_{vdc}(j\omega) \approx -180°$ due to the double poles at zero. Therefore, the controller parameters are selected such that $\frac{k_{idc}}{k_{pdc}} < \frac{1}{\tau_k}$. As a result, the phase angle of $l_{vdc}(j\omega)$ increases to a maximum value $\delta_m^{vdc} = sin^{-1}\left(\left(1 - \tau_k\frac{k_{idc}}{k_{pdc}}\right)\Big/\left(1 + \tau_k\frac{k_{idc}}{k_{pdc}}\right)\right)$ at a certain frequency $\omega_m^{vdc} = \sqrt{2k_{pdc}/\tau_k C_{dc}}$, and then asymptotically decreases to approach $-180°$. The cross-over frequency (ω_c^{vdc}) is selected as ω_m^{vdc} which holds by choosing $k_{pdc} = C_{dc}\omega_c^{vdc}$ such that $|l_{vdc}(j\omega_c^{vdc})| = |l_{vdc}(j\omega_m^{vdc})| = 1$, and hence δ_m^{vdc} becomes the phase margin. By solving the preceding equations, the parameters of the dc-link voltage controller can be determined [31]-[32].

2) *Regulation of the PCC Utility-Grid Voltage:*

As shown in (14), a PI ac voltage controller ($K_{ac}(s) = k_{pac} + k_{iac}/s$) is used to regulate the PCC voltage $\bar{v}_f$ by generating I_{cq}^{*} that corresponds to the required reactive power to maintain a unity PCC voltage. The parameters tuning of $K_{ac}(s)$ is similar to the design of the dc voltage controller in (12).

$$I_{cq}^{*} = -\left(V_{fd}^{*} - V_{fd}^{c}\right)K_{ac}(s) \tag{14}$$

As shown in Fig. 1 and (15), the injected currents to the utility-grid are controlled using a PI ac current controller ($K_i(s) = k_{pi} + k_{ii}/s$).

$$\bar{v}_c^{c} = (\bar{\imath}_c^{*} - \bar{\imath}_c^{c})K_i(s) + j\omega^{\circ}L_f\bar{\imath}_c^{c} + \bar{v}_f^{c} \tag{15}$$

where $j\omega^{\circ}L_f\bar{\imath}_c^{c}$ and $\bar{v}_f^{c}$ are the decoupling and the feedforward loop, respectively. The current controller $K_i(s)$ is designed following the approach described for $G_i(s)$ in (5).

It should be noted that the measured ac quantities, i.e., i_c and v_f, are transformed to the converter reference frame whereas the controller output signals, i.e., v_c, should be retransformed to the grid reference frame to accurately model the influence of the PLL on the system dynamics [30]. The frame transformation is mathematically represented in (16), assuming the angle difference between the two frames is very small such that $\cos\delta \approx 1$ and $\sin\delta \approx 0$.

$$\begin{aligned} \bar{\imath}_c^{c} &= (1 - j\delta)\bar{\imath}_c, \\ \bar{v}_f^{c} &= (1 - j\delta)\bar{v}_f, \\ \bar{v}_c &= (1 + j\delta)\bar{v}_c^{c} \end{aligned} \tag{16}$$

where the superscript "c" denotes the converter reference-frame. The system parameters are all included in Appendix B.

III. Small-Signal Modeling and Stability Analysis

The small-signal model has been developed considering the models of the system components in Section II. The complete state-space model of the entire system comprises 20 states and is given in (17).

$$[\Delta\dot{x}] = [A][\Delta x] \tag{17}$$

where Δx is the states vector, shown at the bottom of this page, and T denotes the matrix transpose; A is the state-matrix and is given in Appendix C. The states ($\Delta\gamma_{id}$, $\Delta\gamma_{iq}$), $\Delta\gamma_s$, ($\Delta\varphi_{id}$, $\Delta\varphi_{iq}$), $\Delta\varphi_{vdc}$, $\Delta\varphi_{vac}$, and ($\Delta\delta$, $\Delta\varphi_{\delta}$), represent the integral terms of the VSR current and speed controllers, the VSI current, dc voltage, ac voltage controllers, and the PLL control loops, respectively.

A. Dominant Eigenvalues

Referring to Table I, the states of the speed and current controller of the VSR, i.e. $\Delta\gamma_s$, $\Delta\gamma_{id}$, and $\Delta\gamma_{iq}$, influence the

$$\Delta x = \left[\Delta I_{sd}\ \ \Delta I_{sq}\ \ \Delta\omega_r\ \ \Delta\gamma_{id}\ \ \Delta\gamma_{iq}\ \ \Delta\gamma_s\ \ \Delta I_{cd}\ \ \Delta I_{cq}\ \ \Delta I_{gd}\ \ \Delta I_{gq}\ \ \Delta v_{fd}\ \ \Delta v_{fq}\ \ \Delta\varphi_{id}\ \ \Delta\varphi_{iq}\ \ \Delta\varphi_{vdc}\ \ \Delta\varphi_{vac}\ \ \Delta\delta\ \ \Delta\varphi_{\delta}\ \ \Delta V_{dc}^{2}\ \ \Delta I_{pv}\right]^{T}$$

This article has been accepted for publication in a future issue of this journal, but has not been fully edited. Content may change prior to final publication. Citation information: DOI 10.1109/TSTE.2019.2890828, IEEE Transactions on Sustainable Energy

most dominant Eigenvalues and hence drive the transient performance of the hybrid system. Moreover, the state of the ac voltage controller of the VSI, i.e., $\Delta\varphi_{vac}$, has a significant impact on the system stability. However, the migration of the dominant modes is less likely to occur because their location is correlated to the controllers parameters which are typically constant under different modes of operation.

TABLE I. EIGENVALUES OF THE PROPOSED HYBRID SYSTEM

EIGEN VALUES	INFLUENCING STATE(S)
$\lambda_1 = -2148.6$	ΔI_{sd}
$\lambda_2 = -0.52$	$\Delta\gamma_{id}$
$\lambda_3 = -6.7 \times 10^6$	ΔI_{pv}
$\lambda_{4,5} = -56.78 \pm j42100$	$\Delta I_{gd}, \Delta I_{gq}, \Delta v_{fd}, \Delta v_{fq}$
$\lambda_{6,7} = -62.46 \pm j41400$	$\Delta I_{gd}, \Delta I_{gq}, \Delta v_{fd}, \Delta v_{fq}$
$\lambda_8 = -8460$	$\Delta I_{cd}, \Delta V_{dc}^2$
$\lambda_9 = -4180$	ΔI_{cq}
$\lambda_{10} = -2130$	ΔI_{sq}
$\lambda_{11,12} = -139.24 \pm j59.93$	$\Delta\varphi_{vdc}, \Delta V_{dc}^2$
$\lambda_{13} = -162.31$	$\Delta\delta$
$\lambda_{14} = -18.93$	$\Delta\omega_r$
$\lambda_{15} = -20$	$\Delta\varphi_{\delta}$
$\lambda_{16} = -2.45$	$\Delta\gamma_s$
$\lambda_{17} = -0.087$	$\Delta\varphi_{vac}$
$\lambda_{18} = -0.52$	$\Delta\gamma_{iq}$
$\lambda_{19} = -10$	$\Delta\varphi_{id}, \Delta\varphi_{iq}$
$\lambda_{20} = -10$	$\Delta\varphi_{id}, \Delta\varphi_{iq}$

B. Influence of the MPPT$_w$ and MPPT$_s$

Referring to Figs. 2-3, the variation range of the optimal speed (ω_r) and dc-voltage (V_{dc}) to maintain the maximum power extraction at different wind speeds and solar irradiance levels is 0.501-to-1.0p.u. and 0.997-to-1.012p.u., respectively. As expected from the participation factor analysis in Table I, the states ΔV_{dc}^2 and $\Delta\omega_r$ influence the relatively highly-damped Eigenvalues, i.e., $\lambda_{11,12}$ and λ_{14}, respectively. Therefore, the variations of the operating points following the MPPT$_w$ and MPPT$_s$ has a minimal influence on the system stability.

IV. EVALUATION RESULTS

A time-domain simulation model for the hybrid system in Fig. 1 is developed under the Matlab/Simulink® environment to evaluate the validity and the performance of the system. The wind and PV generators are rated at 2.0 and 0.9 MVA, respectively. The complete model entities are built using the SimPowerSystem® toolbox. The VSCs are simulated using average-model-based blocks. The simulation type is discrete with a sample time of 50 μs.

In the following subsections, the proposed wind-PV co-generator is subjected to theoretical challenging operating conditions which might not occur in the realty, e.g., large step variations in the wind speed and the solar irradiance levels, and three-phase-to-ground (3PG) faults conditions. These worst-case scenarios are applied to challenge the system stability and show the effectiveness of the designed controllers.

A. Small-Signal Model Verification

The accuracy of the small-signal state-space model in (17) is validated in Fig. 4 following a 5% step increase in V_{dc} at $t = 1.0$ s. In this particular scenario, a lightly damped response has been induced by increasing the bandwidth of the dc-link voltage controller of the VSI so that the model can be easily validated.

For an eigenvalue $\lambda = -\sigma \pm j\omega_\lambda$, the frequency of oscillation is ω_λ [in rad/s] whereas the envelope of the oscillatory response decays following the exponential function $A\exp(-\sigma t)$, where A is the amplitude of the oscillation and t is the time in seconds. The yielded dominant lightly-damped mode is $\lambda = -73.03 \pm j251.7$. Referring to Fig. 4, the frequency of the oscillation of the lightly-damped response is 247.4 rad/s whereas the oscillatory response decays following a close match to $A\exp(-73.03t)$. This implies the accurate development of the small-signal model in (17).

B. Wind-PV Cogeneration

The cogeneration of the wind and PV energy is investigated following different weather conditions. As shown in Fig. 5, the wind speed increases from 8.4 to 10.8, then drops to 7.2, and finally increases to 12m/s at t =2, 4, and 6s, respectively. The solar irradiance level decreases from 1 to 0.8, and then to 0.4, and finally increases to $0.6kW/m^2$, at t =3, 5, and 6s, respectively.

Following Figs. 2-3, the MPPT$_w$ and MPPT$_s$ generate the optimal ω_r^* and V_{dc}^*. The corresponding variables are then regulated using (4) and (12), as shown in Figs. 6(a)-(b), respectively. During the entire operating range, both ω_r and V_{dc} are highly damped which is reflected on the generated wind and PV power as depicted in Figs. 6(c)-(d), respectively, and the injected current to the utility-grid as in Fig. 6(e).

For further investigation, the maximum wind power, i.e., 2MW, and a PV power of 0.568MW are generated at $t = 6.0$ s where the dc-link stability is preserved with a maximum overshoot of 0.06 p.u. as shown in Fig. 6(b). Under all conditions, a unity PCC voltage is maintained following (14), as shown in Fig. 6(f).

The designed vector controllers for the VSR and the VSI do not saturate the generated PWM, as shown in Figs. 6(g)-(h), respectively, where the variable frequency operation of the VSR is clearly noted.

C. Wind-Only Generation

During the night-time or at low-irradiance conditions, the PV generator provides a zero power to the utility-grid. Under this condition, the dc-link voltage is regulated to the minimum value. As shown in Fig. 7(a), the dc-link voltage drops to 0.858p.u. at $t = 2.0$ s as the PV power generation drops to 0, and is restored back to 1.0 p.u. at $t = 3.0$ s when the PV power is generated. The corresponding wind and PV power as well as the injected ac current to the utility-grid are shown in Figs. 7(b)-(c), respectively. Note that a blocking diode is usually connected in series with each PV string to prevent reverse current flow at the low irradiance levels.

D. PV-Only Generation

The wind speed is assumed to be less than the cut-off speed, and hence the majority of the generated wind power is consumed in the system losses. Therefore, the PMSG operates in the braking mode and the rotor is brought to a stand-still by mechanical means.

This article has been accepted for publication in a future issue of this journal, but has not been fully edited. Content may change prior to final publication. Citation information: DOI 10.1109/TSTE.2019.2890828, IEEE Transactions on Sustainable Energy

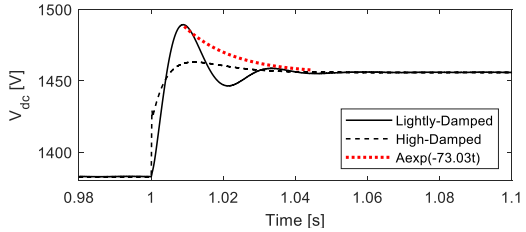

Fig .4. The step response of the dc-link voltage to verify the developed small-signal model in (17).

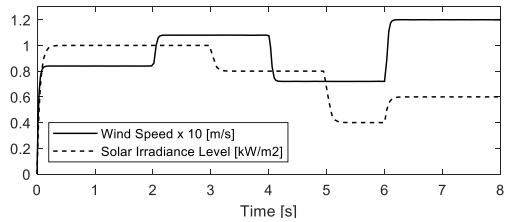

Fig. 5. Wind speed and solar irradiance levels.

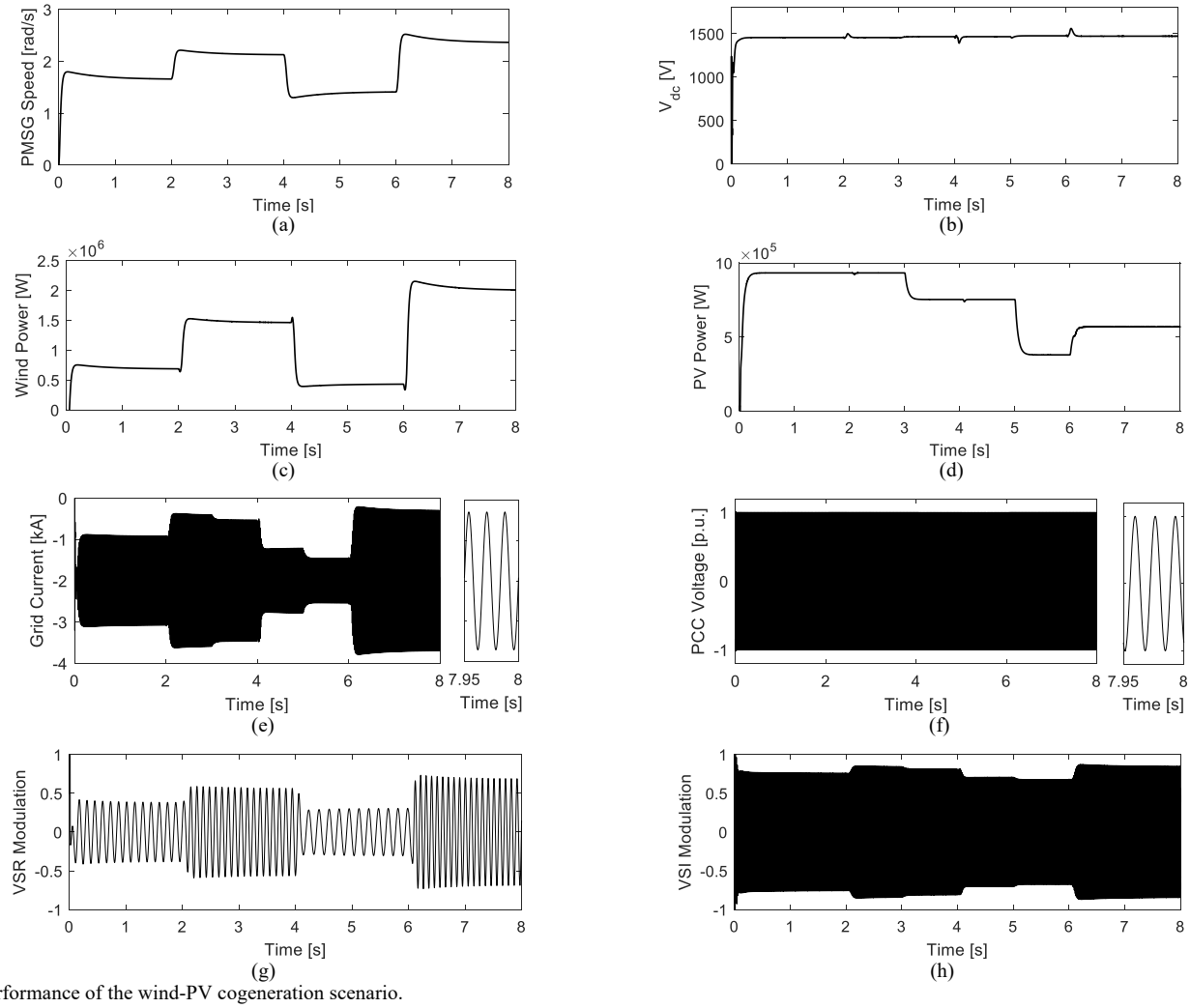

Fig .6. Performance of the wind-PV cogeneration scenario.

As shown in Fig. 8(a), the rotor speed (ω_r) drops from 1 p.u. to 0, and then increases back to 1p.u. at $t = 2$ and 3s, respectively. This corresponds to a sudden change in the generated wind power and injected grid current as shown in Figs. 8(b)-(c), respectively. In spite of the challenging operating scenario, the system stability is maintained.

E. Wind-PV Cogeneration under Faults Conditions

Converter-based distributed generation units roughly contribute by the rated currents under the short circuit conditions. Therefore, and due to the increased penetration of the renewable energy resources to the electrical grids, some utilities have enforced the fault-ride through of power converters [33]. Accordingly, the distributed generation units must not disconnect during fault conditions with a voltage drop down to 0 p. u. that continues to less than or equal to 150 ms (9 cycles for 60Hz systems).

In this operational scenario, the proposed wind-PV cogeneration system is investigated for the fault-ride-through capabilities. The PCC in Fig. 1 has been subjected to a 3PG fault at $t = 4\,\mathrm{s}$ for 4.0 cycles. Further, the VSCs have been implemented in the Simulink model using pulse-width-modulated switching blocks.

Fig. 9 shows the performance of the dc-link voltage and the utility-grid current under the 1.0 p.u. and 0.5 p.u wind power generation whereas the PV power generation is maintained at 1.0 p.u.

This article has been accepted for publication in a future issue of this journal, but has not been fully edited. Content may change prior to final publication. Citation information: DOI 10.1109/TSTE.2019.2890828, IEEE Transactions on Sustainable Energy

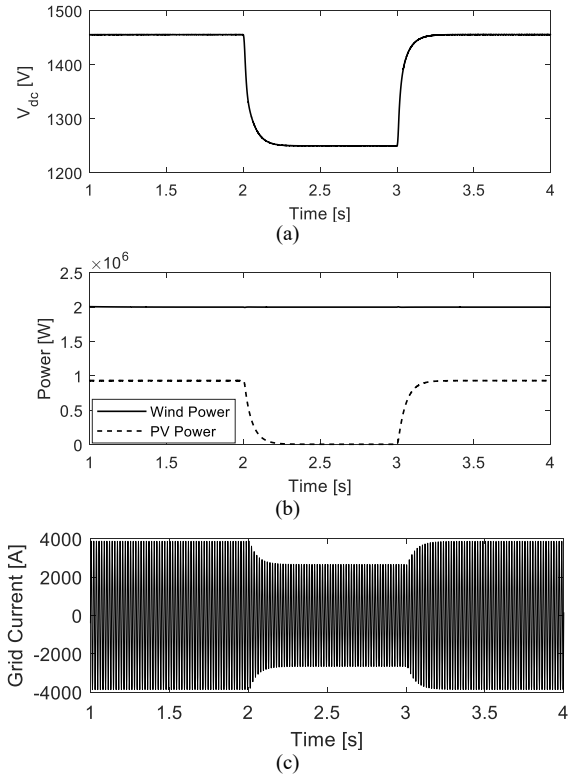

Fig .7. System performance at the wind-only generation scenario.

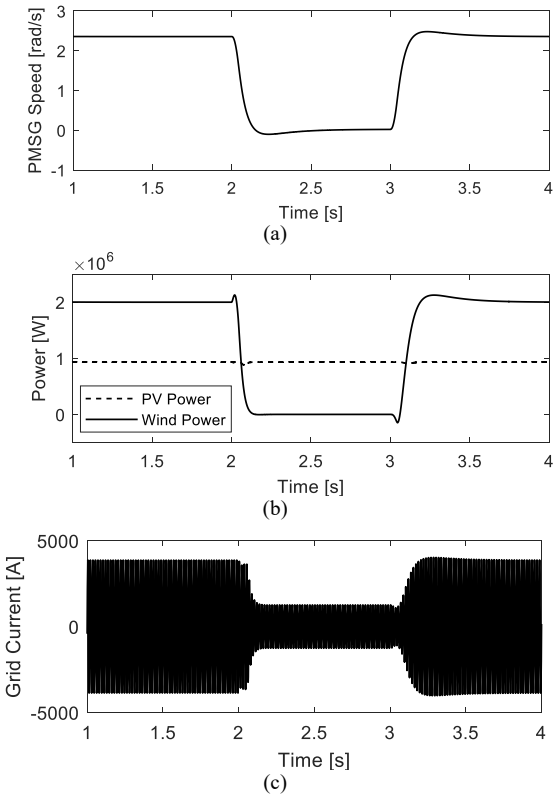

Fig .8. System performance at the PV-only generation scenario.

At 1.0 p.u. wind and PV power generation, and following the clearance of the 3PG fault, the dc-link voltage stability is violated whereas the quality of the injected ac current is degraded to a total-harmonic-distortion (THD) of 8.75%. On the contrary, the response with the 0.5 and 1.0 p.u. wind and PV power generation, respectively, reflects a stable dc-link voltage and a better current quality of a THD of 3.61%. This implies that the wind generator is associated with the system instabilities under the utility-grid faults conditions.

The fault conditions are associated with a sudden drop in the PCC voltage that hinders the maximum power transfer from the dc-link to the grid. As the input wind power is driven by a relatively slow mechanical system, the wind generator keeps injecting the maximum wind power into the dc-link capacitor during the fault conditions. Therefore, the dc-link input power becomes significantly higher than the output power and so the dc-link voltage increases, as shown in Fig. 9(a) [at 1 p.u. wind power]. On the contrary, the PV generator does not contribute to the dc-link voltage instabilities under the fault conditions. The increased dc-link voltage pushes the operating point of the PV array beyond the maximum power point. As shown in Fig. 3, as the PV array voltage exceeds the MPPT operating point, the generated PV power is naturally decreased, and so the PV array does not contribute to the fault currents. The PV generator has self-healing capabilities under the utility-grid faults conditions.

In literature, the protection against the fault conditions in the wind generators is achieved by activating the following protection schemes [34]; 1) using a braking resistance in parallel to the dc-link capacitor of the BtB VSCs so that the generated wind power can be dissipated during the faults. 2) using the pitch angle control so that the wind turbine blades are twisted to reduce the amount of wind power extraction, and hence the mechanical torque input to the wind turbine is reduced.

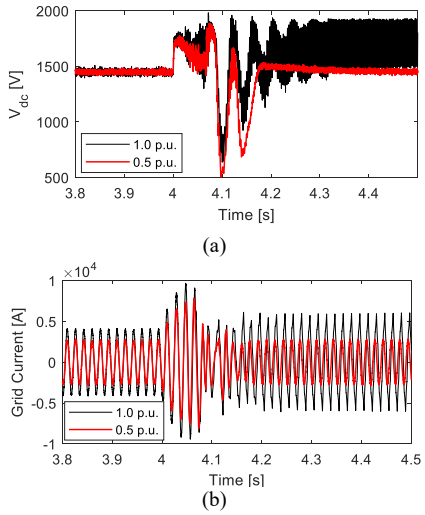

Fig. 9. The system response to a 3PG fault at $t =$ 4.0 s for 4.0 cycles – 1.0 and 0.5 p.u. wind power generation with 1.0 p.u. PV power generation.

Note that both protection schemes can be used so that the braking resistance provides a quick damping till the mechanical pitch controller is activated. Fig. 10 shows the system performance when the preceding fault protections are implemented under 1.0 p.u. wind and PV power generation. The increase of the dc-link voltage has been limited whereas the injected ac current to the grid is maintained stable. The fault-ride through has been achieved by electrically dissipating the extra wind power into the braking resistance till the wind power input is mechanically suppressed using the pitch angle control.

For further investigations, the system performance under the single-phase-to-ground (1PG) fault conditions is investigated in Fig. 11. It is clear that the 1PG fault is not detrimental to the system performance as compared to the 3PG faults in Fig. 9.

This article has been accepted for publication in a future issue of this journal, but has not been fully edited. Content may change prior to final publication. Citation information: DOI 10.1109/TSTE.2019.2890828, IEEE Transactions on Sustainable Energy

However, the protected scheme reflects a more damped dc-link response as compared to the unprotected case.

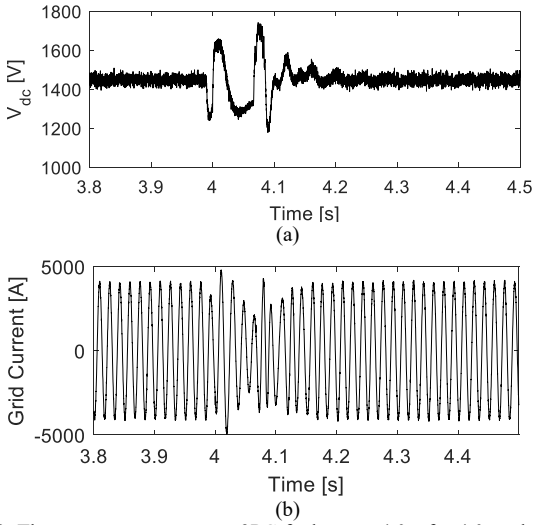

Fig. 10. The system response to a 3PG fault at t = 4.0 s for 4.0 cycles – 1.0 p.u. wind and solar power generation with the implemented fault protection schemes.

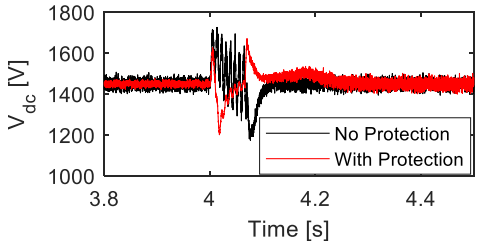

Fig. 11. The system response to a 1PG fault at t = 4.0 s for 4.0 cycles – 1.0 p.u. wind and solar power generation with and without the fault protection schemes.

F. Robustness against Parameters Variations

It is shown in Fig. 5 that the system performance is stable under the wide variation range of operating points. In this section, the system performance is evaluated against the parameters variations.

The short-circuit-ratio (SCR) is a quantity characterizing the stiffness of the utility-grid, where SCR is the ratio of the short-circuit capacity of the utility-grid at the PCC to the rated dc power of the interconnected power converter. In this paper, the utility-grid is originally assumed strong with SCR=15 [results shown in Fig. 5]. In this section, the SCR has decreased to 4.0 and 2.3 to challenge the interconnected converter, as shown in Fig. 12. The PV power is maintained at 1.0 p.u. whereas the wind power is subjected to a step increase from 0.5 to 1.0 p.u. at t =1s. The system response is stable at the wide variation range of SCR values from SCR=15 to SCR=4 as shown in Figs. 5 and 11, respectively. However, the system becomes unstable at SCR=2.3 due to the interactions with the PLL dynamics at the very weak grid conditions [7].

Under the same operating conditions, the influence of the variations of C_f on the PCC voltage is investigated in Fig. 13. As shown, the THD of the PCC voltage increases from 0.05% to 9.8% at 1.25 and 1.5C_f, respectively. In spite of using simple PI controllers for the proposed system, the results in Figs 12-13 indicate a reasonable robustness against the parameters variations.

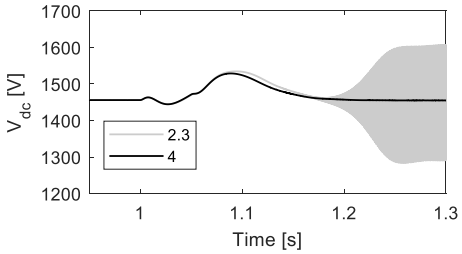

Fig. 12. The dc-link voltage response at different values of SCR – 1.0 p.u. PV power and a step change of the wind power from 0.5 to 1.0 p.u. at t =1s.

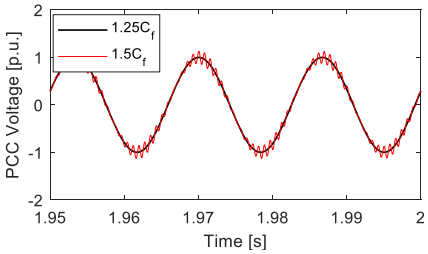

Fig. 13. The PCC voltage response at different values of C_f.

V. Conclusion

This paper has presented the wind-PV cogeneration systems using vector-controlled grid-connected BtB VSCs. The VSR at the wind generator-side is responsible for extracting the maximum wind power following the wind speed variations. On the utility-grid side, the roles of the VSI are to extract the maximum PV power from the PV generator, achieve the balance between the input-output powers across the dc-link capacitor, and to maintain a unity PCC voltage under different modes of operation. A small-signal stability analysis has been conducted for the entire system. The proposed system has the following advantages; 1) the increased reliability and efficiency due to the combined wind and PV generators. 2) the independent MPPT extraction as the VSR and VSI are solely responsible for extracting the wind and PV powers, respectively. 3) the regulation of the dc-link voltage under all operating conditions is maintained by the VSI and hence a better damped performance is yielded. 4) simple system structure and controllers design. 5) fault-ride through can be achieved using existing protection schemes. A well-damped performance has been presented using time-domain simulations results under the Matlab/Simulink® environment.

Appendix A

Model of the PV Generator

$$I_{pv} = N_p\left(\frac{S}{S_r}[I_{sc} + \alpha_i(t - t_r)] - I_o\left[exp\left\{\frac{V_D q}{n_s KAt}\right\} - 1\right] - \frac{V_D}{R_{sh}}\right),$$

$$V_D = \frac{V_{pv} + I_{pv}\left(\frac{N_s}{N_p}\right)R_{se}}{N_s}, I_o = I_{or}\left(\frac{t}{t_r}\right)^3 exp\left\{\frac{te_g q}{KAt}\left(\frac{1}{t_r} - \frac{1}{t}\right)\right\}.$$

where S and S_r are the actual and reference solar irradiance levels, I_{sc} is the short-circuit current of the PV module, α_i is the temperature coefficient, t and t_r are the actual and reference temperature in Kelvin, I_o and I_{or} are the reverse saturation current at the operating and reference temperature, V_D is the internal diode voltage of the PV module, q is the unit charge, K is the Boltzmann's constant, A is the ideality factor, R_{sh} and R_{se} are the equivalent shunt and series resistance of the PV array, e_g is the band-gap energy of the PV cell; n_s is the number of PV cells; N_s is the number of series connected modules; N_p is the number of parallel strings in the PV array.

This article has been accepted for publication in a future issue of this journal, but has not been fully edited. Content may change prior to final publication. Citation information: DOI 10.1109/TSTE.2019.2890828, IEEE Transactions on Sustainable Energy

APPENDIX B

System Parameters

- *PMSG*: $R_s = 0.821\text{m}\Omega$, $L_s = 1.5731\text{mH}$, $\mathcal{P} = 26$, $\psi = 5.8264$ Wb, $J = 32166$ kg. m^2.
- *VSR:* $F_{sw} = 3420Hz$, $G_s(s) = 3000 + 6500/s$, $G_i(s) = 3.38 + 1.76/s$, and $H = 1$.
- *PV*: $N_p = 83$, $N_s = 59$, $n_s = 50$, $R_{dc} = 0.125$ mΩ, $L_{dc} = 0.34$ μH.
- *DC-Link*: $C_{dc} = 4.7$ mF.
- *VSI:* $F_{sw} = 3420Hz$, $R_f = 3$ mΩ, $L_f = 0.3$ mH, $C_f = 60$ μF, $K_\delta(s) = 180 + 3200/s$, $K_{dc}(s) = 1 + 100/s$, $K_{ac}(s) = 0.001 + 24/s$, and $K_i(s) = 1.289 + 12.89/s$.
- *Utility-Grid:* $v_f = 600\text{V}$, $MVA_{sc} = 100\text{MVA}$, $X/R\ Ratio = 10$.

APPENDIX C

State-Space Model of the Hybrid Wind-Solar System

$A = [A_1 \quad A_2]$ which are defined in the next page.

REFERENCES

[1] Renewable Energy Policy Network for the 21st Century, "Advancing the global renewable energy transition," REN21 Secretariat, Paris, France, 2017 [Available Online].

[2] F. Blaabjerg, Z. Chen, and S. B. Kjaer, "Power electronics as efficient interface in dispersed power generation systems," *IEEE Trans. Power Electron.*, vol. 19, no. 5, pp. 1184-1194, 2004.

[3] J. Carrasco et al., "Power-electronic systems for the grid integration of renewable energy sources-a survey," *IEEE Trans. Ind. Electron.*, vol. 53, no. 4, pp. 1002-1016, 2006.

[4] A. Yazdani and P. P. Dash, "A control methodology and characterization of dynamics for a photovoltaic (PV) system interfaced with a distribution network," *IEEE Trans. Power Del.*, vol. 24, no. 3, pp. 1538-1551, 2009.

[5] L. Nousiainen, J. Puukko, A. Maki, T. Messo, J. Huusari, J. Jokipii. J. Viinamaki, D. Lobera, S. Valkealahti, and T. Suntio, "Photovoltaic generator as an input source for power electronic converters," *IEEE Trans. Power Electron.*, vol. 28, no. 6, pp. 3028-3038, 2013.

[6] Nicholas Strachan, and D. Jovcic, "Stability of a variable-speed permanent magnet wind generator with weak ac grids," *IEEE Trans. Power Del.*, vol. 25, no. 4, pp.2279-2788, 2010.

[7] P. Mitra, L. Zhang, and L. Harnefors, "Offshore wind integration to a weak grid by VSC-HVDC links using power-synchronization control - a case study," *IEEE Trans. Power Del.*, vol. 29, no. 1, pp. 453-461, 2014.

[8] Y. Wang, J. Meng, X. Zhang and L. Xu, "Control of PMSG-based wind turbines for system inertial response and power oscillation damping," *IEEE Trans. Sustain. Energy*, vol. 6, no. 2, pp. 565-574, 2015.

[9] F. Giraud, "Analysis of a utility-interactive wind-photovoltaic hybrid system with battery storage using neural network," Ph.D. dissertation, Univ. Mass., Lowell, 1999.

[10] L. Xu, X. Ruan, C. Mao, B. Zhang, and Y. Luo, "An improved optimal sizing method for wind-solar-battery hybrid power system," *IEEE Trans. Sustain. Energy*, vol. 4, no. 3, pp. 774-785, 2013.

[11] S. Sarkar and V. Ajjarapu, "MW resource assessment model for a hybrid energy conversion system with wind and solar resources," *IEEE Trans. Sustain. Energy*, vol. 2, no. 4, pp. 383-391, 2011.

[12] Y.-M. Chen, Y.-C. Liu, S.-C. Hung, and C.-S. Cheng, "Multi-input inverter for grid-connected hybrid PV/wind power system," *IEEE Trans. Power Electron.*, vol. 22, no. 3, pp. 1070-1077, 2007.

[13] S. Bae, and A. Kwasinski, "Dynamic modeling and operation strategy for microgrid with wind and photovoltaic resources," *IEEE Trans. Smart Grid*, vo. 3, no. 4, pp. 1867-1876, 2012.

[14] B. Mangu, S. Akshatha, D. Suryanarayana, and B. G. Fernandes, "Grid-connected PV-wind-battery-based multi-input transformer-coupled bidirectional dc-dc converter for household applications," *IEEE Trans. Emerg. Sel. Topics Power Electron.*, vol. 4, no. 3, pp. 1086-1095, 2016.

[15] P. Shanthi, G. Uma, and M. S. Keerthana, "Effective power transfer scheme for a grid connected hybrid wind/photovoltaic system," *IET Renew. Power Gener.*, vol. 11, no. 7, pp. 1005-1017, 2017.

[16] T. Hirose and H. Matsuo, "Standalone hybrid wind-solar power generation system applying dump power control without dump load," *IEEE Trans. Ind. Electron.*, vol. 59, no. 2, pp. 988-997, 2012.

[17] K. Kant, C. Jain, and B. Singh, "A Hybrid diesel-wind-pv based energy generation system with brushless generators," *IEEE Trans. Ind. Inform.*, vol. 13, no. 4, pp. 1714-1722, 2017.

[18] U. Kalla, B. Singh, S. Murthy, C. Jain and K. Kant, "Adaptive sliding mode control of standalone single-phase microgrid using hydro, wind and solar pv array based generation," *IEEE Trans. Smart Grid*, in press.

[19] A. Merabet, K. Ahmed, H. Ibrahim, R. Beguenane, and A. Ghias, "Energy management and control system for laboratory scale microgrid based wind-pv-battery," *IEEE Trans. Sustain. Energy*, vol. 8, no. 1, pp. 145-154, 2017.

[20] M. Meiqin, S. Jianhui, L. Chang, Z. Guorong and Z. Yuzhu, "Controller for 1kW-5kW wind-solar hybrid generation systems," *Canadian Conf. on Electrical and Computer Engineering*, Niagara Falls, ON, 2008, pp. 1175-1178.

[21] A. Hamadi, S. Rahmani, K. Addoweesh and K. Al-Haddad, "A modeling and control of DFIG wind and PV solar energy source generation feeding four wire isolated load," *IECON 2013 - 39th Annual Conf. of the IEEE Ind. Electron. Society, Vienna*, 2013, pp. 7778-7783.

[22] S. Daniel and N. Ammasai Gounden, "A novel hybrid isolated generating system based on PV fed inverter-assisted wind-driven induction generator," *IEEE Trans. Energy Convers*., vol. 19, no. 2, pp. 416-422, 2004.

[23] P. E. Bett and H. E. Thornton, "The climatological relationships between wind and solar energy in Britain," *Renewable Energy*, vo. 87, no. 1, pp. 96-110, 2016.

[24] S. Shanghavi, W. M. Grady, and B. Schwarz, "Evaluating the impact of wind turbine shadows on an integrated wind and solar farm," *2012 3rd IEEE PES ISGT Europe*, Berlin, 2012, pp. 1-6.

[25] J. Zhang, X. Xie, D. Jiao and Z. Qian, "Stability problems and input impedance improvement for cascaded power electronic systems," in *Proc. APEC*, 2004, pp. 1018-1024 vol.2.

[26] A. Radwan, "Modeling, analysis and stabilization of converter-dominated power distribution grids", M.Sc. thesis, Univ. of Alberta, Edmonton, 2012.

[27] D. Salomonsson, L. Söder, and A. Sannino, "Projection of low-voltage dc microgrid," *IEEE Trans. Power Del.*, vol. 24, no. 3, pp.1045-1053, 2009.

[28] Mitsubishi, "PV-UD190MF5," Mitsubishi, San Francisco, CA, USA, 2007.

[29] ABB Solar Inverters, "PVS980," ABB, 2018.

[30] L. Harnefors, M. Bongiorno, and S. Lundberg, "Input-admittance calculation and shaping for controlled voltage-source converters," *IEEE Trans. Ind. Electron.*, vol. 54, no. 6, pp. 3323-3334, 2007.

[31] A. Yazdani and R. Iravani, Voltage-sourced converters in power systems – modeling, control, and applications, John Wiley & Sons, New Jersey, 2010.

[32] A. Radwan, Y. Mohamed, and E. El-Sadaany, "Assessment and performance evaluation of DC-side interactions of voltage-source inverters interfacing renewable energy systems," *Sustainable Energy, Grids and Networks Journal*, vol. 1, pp. 28-44, 2015.

[33] E. Troester, "New German grid codes for connecting PV systems to the medium voltage power grid," in *Proc. 2nd Int. Workshop on Concentrating Photovoltaic Power Plant*, pp. 1 – 4.

[34] I. Abdelsalam, G. Adam, B. Williams, "Current source back-to-back converter for wind energy conversion systems," *IET Renew. Power Gener*., vol. 10, no. 10, pp. 1552-1561, 2016.

$$A_1 = \begin{bmatrix}
\frac{-1}{L_s}(R_s+g_{pi}) & 0 & \mathcal{P}I_{sq}^{\circ} & \frac{1}{L_s} & 0 & 0 & 0 & 0 & 0 & 0 \\
0 & \frac{-1}{L_s}(R_s+g_{pi}) & \frac{-g_{pi}g_{ps}}{L_s}+\frac{\mathcal{P}\psi}{L_s}(H-1) & 0 & \frac{1}{L_s} & \frac{g_{pi}}{L_s} & 0 & 0 & 0 & 0 \\
0 & \frac{3}{2}\frac{\mathcal{P}\psi}{J} & 0 & 0 & 0 & 0 & 0 & 0 & 0 & 0 \\
-g_{ii} & 0 & 0 & 0 & 0 & 0 & 0 & 0 & 0 & 0 \\
0 & -g_{ii} & -g_{ps}g_{ii} & 0 & 0 & g_{ii} & 0 & 0 & 0 & 0 \\
0 & 0 & -g_{is} & 0 & 0 & 0 & 0 & 0 & 0 & 0 \\
0 & 0 & 0 & 0 & 0 & 0 & \frac{-1}{L_f}(R_f+k_{pi}) & 0 & 0 & 0 \\
0 & 0 & 0 & 0 & 0 & 0 & 0 & \frac{-1}{L_f}(R_f+k_{pi}) & 0 & 0 \\
0 & 0 & 0 & 0 & 0 & 0 & 0 & 0 & -\frac{R_g}{L_g} & \omega^{\circ} \\
0 & 0 & 0 & 0 & 0 & 0 & 0 & 0 & -\omega^{\circ} & -\frac{R_g}{L_g} \\
0 & 0 & 0 & 0 & 0 & 0 & \frac{1}{C_f} & 0 & -\frac{1}{C_f} & 0 \\
0 & 0 & 0 & 0 & 0 & 0 & 0 & \frac{1}{C_f} & 0 & -\frac{1}{C_f} \\
0 & 0 & 0 & 0 & 0 & 0 & -k_{ii} & 0 & 0 & 0 \\
0 & 0 & 0 & 0 & 0 & 0 & 0 & -k_{ii} & 0 & 0 \\
0 & 0 & 0 & 0 & 0 & 0 & 0 & 0 & 0 & 0 \\
0 & 0 & 0 & 0 & 0 & 0 & 0 & 0 & 0 & 0 \\
0 & 0 & 0 & 0 & 0 & 0 & 0 & 0 & 0 & 0 \\
0 & 0 & 0 & 0 & 0 & 0 & 0 & 0 & 0 & 0 \\
\frac{3}{C_{dc}}(\mathcal{P}\omega_r^{\circ}L_sI_{sq}^{\circ}+V_{sd}^{\circ}) & \frac{3}{C_{dc}}(-g_{pi}I_{sq}^{\circ}+V_{sq}^{\circ}) & \frac{3I_{sq}^{\circ}}{C_{dc}}(\mathcal{P}\psi H-g_{pi}g_{ps}) & 0 & \frac{3I_{sq}^{\circ}}{C_{dc}} & \frac{3g_{pi}I_{sq}^{\circ}}{C_{dc}} & \frac{-3}{C_{dc}}(V_{cd}^{\circ}-k_{pi}I_{cd}^{\circ}+\omega^{\circ}L_fI_{cq}^{\circ}) & \frac{-3}{C_{dc}}(V_{cq}^{\circ}-k_{pi}I_{cq}^{\circ}-\omega^{\circ}L_fI_{cd}^{\circ}) & 0 & 0 \\
0 & 0 & 0 & 0 & 0 & 0 & 0 & 0 & 0 & 0
\end{bmatrix}$$

$$A_2 = \begin{bmatrix}
0 & 0 & 0 & 0 & 0 & 0 & 0 & 0 & 0 & 0 \\
0 & 0 & 0 & 0 & 0 & 0 & 0 & 0 & 0 & 0 \\
0 & 0 & 0 & 0 & 0 & 0 & 0 & 0 & 0 & 0 \\
0 & 0 & 0 & 0 & 0 & 0 & 0 & 0 & 0 & 0 \\
0 & 0 & 0 & 0 & 0 & 0 & 0 & 0 & 0 & 0 \\
0 & 0 & 0 & 0 & 0 & 0 & 0 & 0 & 0 & 0 \\
0 & \frac{k_{p\delta}I_{cq}^{\circ}}{V_{fd}^{\circ}} & \frac{1}{L_f} & 0 & \frac{k_{pi}}{L_f} & 0 & -\left(k_{p\delta}+\frac{k_{pi}}{L_f}\right)I_{cq}^{\circ}+\omega^{\circ}I_{cd}^{\circ} & I_{cq}^{\circ} & \frac{k_{pi}k_{pdc}}{1.5V_{fd}^{\circ}L_f} & 0 \\
\frac{k_{pi}k_{pac}}{L_f} & -\frac{k_{p\delta}I_{cd}^{\circ}}{V_{fd}^{\circ}} & 0 & \frac{1}{L_f} & 0 & \frac{k_{pi}}{L_f} & \left(k_{p\delta}+\frac{k_{pi}}{L_f}\right)I_{cd}^{\circ}+\omega^{\circ}I_{cq}^{\circ}+\frac{1}{L_f}(V_{cd}^{\circ}-V_{fd}^{\circ}) & -I_{cd}^{\circ} & 0 & 0 \\
\frac{1}{L_g} & \frac{k_{p\delta}I_{gq}^{\circ}}{V_{fd}^{\circ}} & 0 & 0 & 0 & 0 & -I_{gq}^{\circ}k_{p\delta} & I_{gq}^{\circ} & 0 & 0 \\
0 & \frac{1}{L_g}-\frac{k_{p\delta}I_{gd}^{\circ}}{V_{fd}^{\circ}} & 0 & 0 & 0 & 0 & I_{gd}^{\circ}k_{p\delta} & -I_{gd}^{\circ} & 0 & 0 \\
0 & \omega^{\circ} & 0 & 0 & 0 & 0 & 0 & 0 & 0 & 0 \\
-\omega^{\circ} & -k_{p\delta} & 0 & 0 & 0 & 0 & V_{fd}^{\circ}k_{p\delta} & -V_{fd}^{\circ} & 0 & 0 \\
0 & 0 & 0 & 0 & k_{ii} & 0 & -k_{ii}I_{cq}^{\circ} & 0 & \frac{k_{ii}k_{pdc}}{1.5V_{fd}^{\circ}} & 0 \\
k_{pac}k_{ii} & 0 & 0 & 0 & 0 & k_{ii} & k_{ii}I_{cd}^{\circ} & 0 & 0 & 0 \\
0 & 0 & 0 & 0 & 0 & 0 & 0 & 0 & \frac{k_{idc}}{1.5V_{fd}^{\circ}} & 0 \\
k_{iac} & 0 & 0 & 0 & 0 & 0 & 0 & 0 & 0 & 0 \\
0 & \frac{k_{p\delta}}{V_{fd}^{\circ}} & 0 & 0 & 0 & 0 & -k_{p\delta} & 1 & 0 & 0 \\
0 & \frac{k_{i\delta}}{V_{fd}^{\circ}} & 0 & 0 & 0 & 0 & -k_{i\delta} & 0 & 0 & 0 \\
\frac{-3}{C_{dc}}(I_{cd}^{\circ}+k_{pi}k_{pac}I_{cq}^{\circ}) & \frac{-3I_{cq}^{\circ}}{C_{dc}} & \frac{-3I_{cd}^{\circ}}{C_{dc}} & \frac{-3I_{cq}^{\circ}}{C_{dc}} & \frac{-3I_{cd}^{\circ}k_{pi}}{C_{dc}} & \frac{-3I_{cq}^{\circ}k_{pi}}{C_{dc}} & \frac{-3}{C_{dc}}(I_{cq}^{\circ}V_{cd}^{\circ}+\omega^{\circ}L_fI_{cd}^{\circ 2}+\omega^{\circ}L_fI_{cq}^{\circ 2}) & 0 & \frac{I_{pv}^{\circ}}{C_{dc}V_{dc}^{\circ}}-\frac{2k_{pi}k_{pdc}I_{cd}^{\circ}}{C_{dc}V_{fd}^{\circ}} & \frac{2V_{dc}^{\circ}}{C_{dc}} \\
0 & 0 & 0 & 0 & 0 & 0 & 0 & 0 & \frac{-1}{2L_{dc}V_{dc}^{\circ}} & \frac{-1}{L_{dc}}\left(R_{dc}+\frac{V_{pv}^{\circ}}{I_{pv}^{\circ}}\right)
\end{bmatrix}$$

Amr Ahmed A. Radwan (S'11-M'16) was born in Cairo, Egypt, on December 27, 1984. He received the B.Sc. degree (hons.) in electrical engineering from Ain Shams University, Cairo, Egypt in 2007; and the M.Sc. and Ph.D. degree in electrical engineering from the University of Alberta, Edmonton, AB, Canada, in 2012 and 2016, respectively. His research interests include the areas of smart active distribution systems and control of power electronic converters.

Dr. Radwan is currently an Assistant Professor at the Engineering and Design Department, Electrical Engineering, Western Washington University, Bellingham, WA, USA. He is a registered Professional Engineer in the Province of Alberta.

Yasser Abdel-Rady I. Mohamed (M'06–SM'11) was born in Cairo, Egypt, on November 25, 1977. He received the B.Sc. (with honors) and M.Sc. degrees in electrical engineering from Ain Shams University, Cairo, in 2000 and 2004, respectively, and the Ph.D. degree in electrical engineering from the University of Waterloo, Waterloo, ON, Canada, in 2008. Since September 2009, he has been the Department of Electrical and Computer Engineering, University of Alberta, Edmonton, Canada, where now he holds the rank of Full Professor. His research interests include dynamics and controls of power converters; grid integration of distributed generation and renewable resources; microgrids; modeling, analysis and control of smart grids; and electric machines and motor drives.

Dr. Mohamed is an Associate Editor of the IEEE Transactions on Industrial Electronics and IEEE Transactions on Power Electronics, and an Editor of the IEEE Transactions on Power Systems and IEEE Transactions on Smart Grid. Dr. Mohamed is a registered Professional Engineer in the Province of Alberta.